

On the Sensitivity of Thermocline Depth and Meridional Heat Transport to Vertical Diffusivity in OGCMs*

DINGMING HU

Joint Institute for the Study of the Atmosphere and Ocean, University of Washington, Seattle, Washington

(Manuscript received 11 April 1995, in final form 5 February 1996)

ABSTRACT

Aimed at a further understanding of the role of vertical diffusivity in determining the vertical structure of the thermocline circulation and meridional heat transport in ocean general circulation models (OGCMs), sensitivity of a box-basin isopycnal ocean model to vertical diffusivity is examined. In constant diffusivity experiments, the model e -folding depth for potential density is proportional to the $1/3$ power of vertical diffusivity, which is in agreement with previous sensitivity studies with the GFDL OGCM. In the experiments with an N^{-1} type of stability-dependent vertical diffusivity, we found that the minimum diffusivity in the vertical is a relevant scale for the stability-dependent diffusivity in describing the sensitivity of the thermocline depth. With the choice of this vertical diffusivity scale, the $1/3$ power law for the constant diffusivity case can be extended to the stability-dependent diffusivity case. Contrary to the previous sensitivity studies, meridional heat transport in the present model is rather insensitive to vertical diffusivity. It is shown that the low sensitivity is mainly due to the different reference temperature and surface anomaly damping rate used in the model's Newtonian cooling parameterization for the surface heat flux. Since sensitivity of the thermocline depth is rather OGCM independent and that of meridional heat transport is dependent on the way surface heat flux is parameterized, the author suggests that vertical diffusivity be tuned to obtain a realistic thermocline. In this regard, the stability-dependent vertical diffusivity is recommended.

1. Introduction

In ocean general circulation models, vertical mixing is a subgrid-scale process that must be parameterized in terms of grid-scale variables. Numerical models are sensitive to the way this is done. Although it is becoming feasible to resolve energy-containing mesoscale eddies in OGCMs, explicit resolution of small-scale turbulent mixing will be beyond the computing capacities in the foreseeable future. Therefore, parameterization of small-scale turbulent mixing and sensitivity of OGCMs to it have been major concerns of ocean observers and modelers (Bryan 1987; Gregg 1987; Muller and Holloway 1989; Cummins et al. 1990).

In OGCMs small-scale turbulent mixing is usually parameterized by vertical eddy diffusivity K_v . In a parameter study with the GFDL ocean model, Bryan (1987) showed that the model is very sensitive to the magnitude of constant vertical diffusivity. The value that results in a reasonable thermocline depth produces too small a meridional heat transport. On the other

hand, the value that gives a reasonable meridional heat transport yields too diffusive a thermocline. Since both the thermocline depth and meridional heat transport are climatically important diagnostic quantities, Bryan stressed that more realistic parameterizations are needed for OGCM improvement. Recent progress in deriving a more realistic parameterization of diapycnal mixing has suggested a stability-dependent vertical diffusivity, inversely proportional to the buoyancy frequency N (Gargett 1984; Moum and Osborn 1986); that is,

$$K_d = a_0 N^{-1}, \quad (1)$$

where a_0 is a constant coefficient. Cummins et al. (1990, hereafter CHG) studied the sensitivity of the GFDL ocean model to this stability-dependent vertical diffusivity, but their results did not lead to an encouraging reduction of the model sensitivity.

In the sensitivity studies of both Bryan and CHG, numerical experiments were carried out under the surface boundary conditions of relaxation to Levitus climatological sea surface temperature (SST) and salinity (SSS). A natural question is "do OGCMs remain sensitive to vertical diffusivity under more realistic surface boundary conditions?" In this paper we examine the sensitivity of a coupled mixed layer–isopycnal coordinate OGCM to vertical diffusivity under more realistic surface boundary conditions. The purpose of this

* Joint Institute for the Study of the Atmosphere and Ocean Contribution Number 320.

Corresponding author address: Dr. Dingming Hu, JISAO, University of Washington, Box 354235, Seattle, WA 98195.

study is to gain a further insight into the role of vertical diffusivity in determining the thermocline depth and meridional heat transport in OGCMs.

2. Model description and experiment design

The model used in this study is that developed by Hu (1991) based on the idealized thermocline-ventilation model of Bleck et al. (1989, BHHK hereafter). Since the model is a coupled mixed layer–isopycnic coordinate OGCM, the model governing equations can be expressed in generalized vertical coordinate s as

$$\left(\frac{\partial \mathbf{v}}{\partial t}\right)_s + \nabla_s \cdot \frac{\mathbf{v}^2}{2} + (\zeta + f)\mathbf{k} \times \mathbf{v} + e^* \frac{\partial \mathbf{v}}{\partial s} + \nabla_s M$$

$$= \frac{1}{\partial p / \partial s} \nabla_s \cdot \left(\nu \frac{\partial p}{\partial s} \nabla_s \mathbf{v} \right) \quad (2)$$

$$\frac{\partial M}{\partial \alpha} = p \quad (3)$$

$$\frac{\partial}{\partial t} \left(\frac{\partial p}{\partial s} \right)_s + \nabla_s \cdot \left(\mathbf{v} \frac{\partial p}{\partial s} \right) + \frac{\partial e^*}{\partial s} = 0 \quad (4)$$

$$\frac{\partial}{\partial t} \left(\theta \frac{\partial p}{\partial s} \right)_s = -\nabla_s \cdot \left(\mathbf{v} \theta \frac{\partial p}{\partial s} \right) + \nabla_s \cdot \left(K_H \frac{\partial p}{\partial s} \nabla_s \theta \right)$$

$$+ \frac{\partial(e^* \theta)}{\partial s} + \frac{\partial}{\partial s} \left(\frac{g^2}{\alpha^2} K_v \frac{\partial \theta}{\partial p} \right) \quad (5)$$

$$\frac{\partial}{\partial t} \left(S \frac{\partial p}{\partial s} \right)_s = -\nabla_s \cdot \left(\mathbf{v} S \frac{\partial p}{\partial s} \right) + \nabla_s \cdot \left(K_H \frac{\partial p}{\partial s} \nabla_s S \right)$$

$$+ \frac{\partial(e^* S)}{\partial s} + \frac{\partial}{\partial s} \left(\frac{g^2}{\alpha^2} K_v \frac{\partial S}{\partial p} \right). \quad (6)$$

Here $\mathbf{v} [= (u, v)]$ is the horizontal velocity vector, p is pressure, $\partial p / \partial s$ is layer thickness in pressure units, $e^* (= s \partial p / \partial s)$ is the generalized vertical velocity, $\zeta [= (\partial v / \partial x)_s - (\partial u / \partial y)_s]$ is the relative vorticity, f is the Coriolis parameter, $M (= gz + p\alpha)$ is the Montgomery streamfunction, $\alpha (= \rho^{-1})$ is the potential specific volume, ν is a lateral eddy viscosity proportional to the large-scale deformation (Smagorinsky 1963), and K_H and K_v are respectively lateral and vertical diffusivities. Vertical momentum mixing is not explicitly included in the momentum equations, but its effect is encompassed in an interface smoothing (BHHK). In the model, a simple nonlinear equation of state by BHHK is used to close the governing equations.

The model governing equations (2)–(6) are basically the same as those of Bleck et al. (1992, BRHS hereafter). The major difference is that BRHS' model does not have the mixing terms associated with vertical diffusivity K_v in Eqs. (5) and (6) and thus is not relevant to our sensitivity study. Due to the absence of K_v ,

e^* is also different between the two models. In the isopycnic interior, $s = \rho$ and $e^* (= \dot{\rho} \partial p / \partial \rho)$ represents a diapycnal velocity. In practice, however, diapycnal velocity is defined as $e \equiv \dot{\rho} \partial z / \partial \rho (= -\alpha e^* / g)$ in that e^* does not have the dimensions of velocity. Based on the definition, diapycnal velocity in the present model can be expressed as (Hu 1991, 1995)

$$e = \frac{g}{N^2} \left[\hat{\alpha} \left[\nabla_\rho \cdot (K_H \nabla_\rho \theta) + \frac{\partial}{\partial z} \left(K_v \frac{\partial \theta}{\partial z} \right) \right] \right.$$

$$\left. - \hat{\beta} \left[\nabla_\rho \cdot (K_H \nabla_\rho S) + \frac{\partial}{\partial z} \left(K_v \frac{\partial S}{\partial z} \right) \right] \right], \quad (7)$$

where

$$\hat{\alpha} = -\frac{1}{\rho_0} \frac{\partial \rho}{\partial \theta} \quad \text{and} \quad \hat{\beta} = \frac{1}{\rho_0} \frac{\partial \rho}{\partial S}$$

are respectively thermal expansion and haline contraction coefficients, and

$$N^2 = g \left(-\hat{\alpha} \frac{\partial \theta}{\partial z} + \hat{\beta} \frac{\partial S}{\partial z} \right)$$

is the buoyancy frequency. Equation (7) can be expressed in the same form as that for dianeutral velocity derived by McDougall (1987). The only difference is that $\hat{\alpha}$ and $\hat{\beta}$ are functions of θ , S , and p for dianeutral velocity but are functions of only θ and S in Eq. (7). Equation (7) shows that diapycnal velocity in the present model is caused by both diapycnal and isopycnic mixing of temperature and salinity in the interior ocean. In contrast, diapycnal velocity in BRHS is only caused by isopycnic mixing of temperature and salinity and is always downward due to the cabbeling effect. Note that vertical mixing and diapycnal velocity associated with it play a crucial role in closing the model thermohaline circulation and determining the model thermocline stratification. Therefore, correct representation of diapycnal mixing and advection processes are the key to carrying out the parameter sensitivity study. In the present model, interior diapycnal diffusive and advective fluxes are computed by the algorithms developed by Hu (1991, 1995), which overcome the difficulties associated with massless isopycnic layers, and assure that the computed fluxes are physically reasonable and mathematically continuous. Except for mass exchanges between isopycnic layers, there is a mass exchange between the mixed layer and the underlying isopycnic layers, which is mainly caused by the mixed layer entrainment/detrainment and free convection processes. In the present model, the mixed layer entrainment/detrainment is predicted by a Kraus–Turner mixed layer model (BHHK 1989; Hu 1991).

The mathematical model formulation is completed by the specification of boundary conditions. At the side walls, no-slip and impermeability conditions are specified for the momentum equations and insulating con-

ditions are specified for the heat and salt conservation equations. The bottom boundary is impermeable and insulating. In addition, a linear drag is specified at the bottom. The air-sea interface in the model is assumed to be a rigid lid to filter out the fast propagating external gravity waves. At the surface, the model is forced by the surface wind stress and heat flux used in BHHK, which varies with season and latitude, and by an $E - P$ type of surface salinity flux, which is a function of latitude only.

In OGCMs total heat flux across the sea surface is usually parameterized in a Newtonian cooling form, which reads

$$Q = \rho c_w \frac{\Delta Z_1}{\tau_R} (T_1 - T_r), \quad (8)$$

where Q is positive upward, c_w is the specific heat of seawater, T_1 is the model SST, T_r is a reference temperature, ΔZ_1 is the top layer thickness of the model, τ_R is a relaxation time scale, and $\Delta Z_1/\tau_R$ is a vertical damping rate for an imposed thermal anomaly at the surface. In Bryan and CHG, $\Delta Z_1/\tau_R$ is set to 2 m day^{-1} and T_r is the observed SST from the Levitus (1982) dataset. According to Haney (1971), T_r is an apparent atmospheric temperature that includes the effects of evaporation and solar radiation. Furthermore, $\Delta Z_1/\tau_R$ is not simply a constant. In the present model, $\Delta Z_1/\tau_R$ and T_r are respectively expressed as

$$\frac{\Delta Z_1}{\tau_R} = c_H \frac{\rho_a c_p}{\rho c_w} U_a \quad (9)$$

$$T_r = T_a - \frac{R}{c_H \rho_a c_p U_a}, \quad (10)$$

where c_H is a dimensionless heat transfer coefficient, ρ_a is the air density, c_p is the specific heat at constant pressure, U_a is wind speed, T_a is a pseudo air temperature, and R is the net radiative heat flux at the sea surface. As shown in (9), $\Delta Z_1/\tau_R$ is a function of wind speed U_a , which varies with latitude and time in the present model. For the model basin, however, latitudinal and seasonal variations of $\Delta Z_1/\tau_R$ are weak, ranging from 0.2 m day^{-1} at 10°N in summer to 0.5 m day^{-1} at 59°N in winter. In (10) the pseudo air temperature T_a is derived from the COADS dataset so that when the model surface temperature T_1 is equal to the observed SST, the model surface heat flux will be identical to the sum of the observed sensible, latent, and radiative heat fluxes (BHHK 1989). Thus, as in Haney (1971), the effects of evaporation and radiation are included in T_r in the present model. If the model is able to simulate the observed SST, the model will reproduce the observed surface heat fluxes.

In the present model the surface salinity flux is given as $(E - P)S_0$, where E and P are the rates of evaporation and precipitation, and S_0 is the basin-averaged salinity. The forcing function $E - P$ is constructed to

qualitatively capture the basic characteristics of the annual mean $E - P$ map for the North Atlantic given by Schmitt et al. (1989) and is expressed as a fourth-order polynomial (Hu 1991)

$$f(y) = a_0(y - y_0)(y - y_1)(1 + a_1y + a_2y^2),$$

where y is the distance from the equator on a Mercator projection and a_0 is a coefficient used to adjust the amplitude of $f(y)$. At y_0 and y_1 , $E - P$ is equal to zero. Coefficients a_1 and a_2 are determined by the following conditions: 1) the residual $E - P$ over the basin equals zero and 2) $E - P$ reaches a minimum at a latitude in the subpolar region. Note that condition 1) is necessary for the model integration to reach an equilibrium state. The $E - P$ function used in this study is plotted in Fig. 1, which shows that $E - P$ is zero at about 10°N and 39°N , and reaches a maximum at about 25°N and a minimum at 57°N . All these features can be reasonably found as the basic characteristics of the annual mean $E - P$ map for the North Atlantic Ocean in Schmitt et al. Quantitatively, however, the peak values of $E - P$ in the subtropics are about one order of magnitude smaller than those shown in the map of Schmitt et al. As pointed out by Schmitt et al. the North Atlantic is an evaporative basin on the whole. The computational domain of the present model does not include the net precipitation zones south of 10°N and north of 60°N in the North Atlantic and thus is even more evaporative. Since precipitation and evaporation must be balanced in the model basin, we can only achieve the balance either by reducing the evaporation rate in the south (Hu 1991) or by increasing the precipitation rate in the north (BRHS 1992). If the later approach is used, the net precipitation in the high latitudes will be about one order larger than the observed, which may drive the model into a regime of internal oscillation. This case is not considered in the present study. We therefore

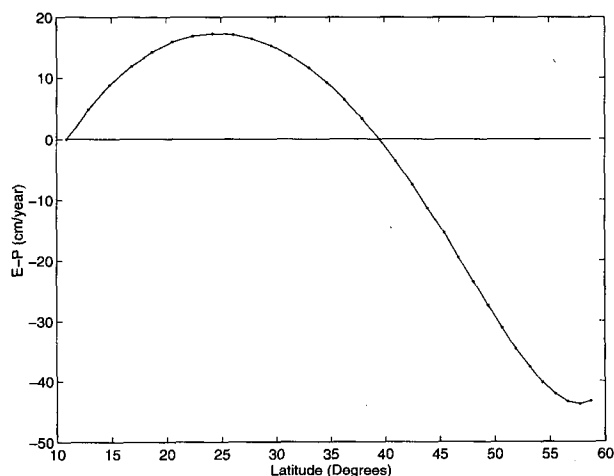


FIG. 1. Evaporation minus precipitation (cm yr^{-1}) as a boundary condition.

adopted the former approach. So the poor match in the amplitude of $E - P$ in the subtropics is the price paid for the basinwide balance of evaporation and precipitation.

The model domain is an idealized ocean basin ranging 64° in longitude and extending from 10°N to 59°N . The governing equations are solved in a regular horizontal mesh on a Mercator projection, which consists of 32×32 grid points with a 2° interval in longitude. The basin depth is 5 km. The vertical structure of the model is represented by a surface mixed layer and five underlying isopycnal-coordinate layers, whose prescribed density values are respectively 26.1, 26.5, 26.9, 27.3, and 27.8 in σ_θ units. In the present model K_H is linearly proportional to the grid size and thus decreases from about $2 \times 10^7 \text{ cm}^2 \text{ s}^{-1}$ in the southernmost grid point to $10^7 \text{ cm}^2 \text{ s}^{-1}$ in the northernmost grid point.

Six numerical experiments have been carried out in this study. All are spun up from a zonally symmetric density structure excerpted from the Levitus (1982) dataset and are run into equilibrium. The experiments are summarized in Table 1. Experiments 1–3 are intended to examine the model sensitivity to the stability-dependent vertical diffusivity, while experiments 4–6 are to examine the sensitivity to the constant vertical diffusivity. In the stability-dependent experiments the proportionality coefficient a_0 [see Eq. (1)] is $5.75 \times 10^{-4} \text{ cm}^2 \text{ s}^{-2}$ (Kraus 1990) in experiment 1, while in experiment 3 it is increased by more than 10 times. In the constant diffusivity experiments, the magnitude of the vertical diffusivity is also varied by one order. A consideration in the design of the experiments is to match vertical diffusivities used in the previous parameter studies carried out with the GFDL ocean model. For instance, the constant diffusivities in experiments 5 and 6 were used by Bryan (1987), and the diffusivities in experiments 2 and 4 were used in CGH (1990). In this way, we are able to not only examine the model response to variations in vertical diffusivity but also make a comparison with the results of the GFDL model.

3. Annual-mean vertical diffusivity

In the stability-dependent vertical diffusivity experiments, K_v itself is part of the model solutions. Since we are studying the model response to variations in K_v , it is helpful to have an impression in the magnitude and distribution of K_v in the stability-dependent experiments. Figure 2 shows the map of annual-mean vertical diffusivity (AMVD) for experiment 3. The other stability-dependent experiments have similar AMVD distributions, and the main difference is in magnitude. Generally speaking, Fig. 2 shows that the AMVD increases with latitude and depth, reflecting that the vertical stratification weakens northward and downward. On the lowest interface (interface 6), the AMVD is highest and is distributed rather uniformly over the ba-

TABLE 1. Summary of K_v values used in the sensitivity experiments.

Experiment	K_v ($\text{cm}^2 \text{ s}^{-1}$)	Length of integration (years)
1	$5.75 \times 10^{-4} N^{-1}$	1000
2	$3 \times 10^{-3} N^{-1}$	900
3	$6 \times 10^{-3} N^{-1}$	900
4	0.3	1000
5	1.0	1000
6	2.5	1100

sin. On the upper isopycnal interfaces the AMVD maps are characterized by interweaving high and low AMVD tongues extending from the western and eastern boundaries. The westward-extending low-AMVD tongues in the low latitudes indicate shoaling of isopycnal surfaces to the east in the upper thermocline, while the low-AMVD tongues in the midlatitudes are located in the isopycnal outcropping zones. The high-AMVD tongues extending from the western boundary current region reflect the shape and extension of a low potential vorticity (PV) water (or mode water) in the isopycnal layers. As shown in Hu (1991), the low-PV water is formed in the winter mixed layer and is detrained into the seasonal thermocline in the later spring and summer. Thus, the low-PV water marks the northern boundary of the permanent thermocline, which is not directly influenced by the seasonal cycle of the mixed layer entrainment and detrainment.

Since the mixed layer entrainment and detrainment are dominant over the small-scale vertical mixing in the seasonal thermocline, it is in the permanent thermocline where the role of vertical diffusivity is most important: it is the only cause for interlayer mass exchange. To give a clear view of the stability-dependent diffusivity distribution with depth, we plot the vertical profiles of AMVD averaged over the area south of 30°N in the model for experiments 1–3 in Fig. 3. From left to right, the solid curves in Fig. 3 are the vertical profiles of the area-averaged AMVD for experiments 1, 2, and 3, and the dashed straight lines indicate the mass-weighted vertical average values within the depth ranges of the vertical profiles. The dots on the solid curves indicate the data points, that is, the values at the depths of the area-averaged isopycnal interfaces. In experiment 1 ($a_0 = 5.75 \times 10^{-4} \text{ cm}^2 \text{ s}^{-2}$), the area-averaged AMVD is about $0.03 \text{ cm}^2 \text{ s}^{-1}$ at the uppermost interface and $0.4 \text{ cm}^2 \text{ s}^{-1}$ at the lowest interface with a vertical average value of $0.18 \text{ cm}^2 \text{ s}^{-1}$. In experiment 3, $a_0 (= 6 \times 10^{-3} \text{ cm}^2 \text{ s}^{-2})$ is more than 10 times that in experiment 1. Correspondingly, vertical diffusivities at all interfaces are also increased by more than ten times, ranging from $0.38 \text{ cm}^2 \text{ s}^{-1}$ at the uppermost interface to $4.16 \text{ cm}^2 \text{ s}^{-1}$ at the lowest interface. The vertical average value is $2.25 \text{ cm}^2 \text{ s}^{-1}$.

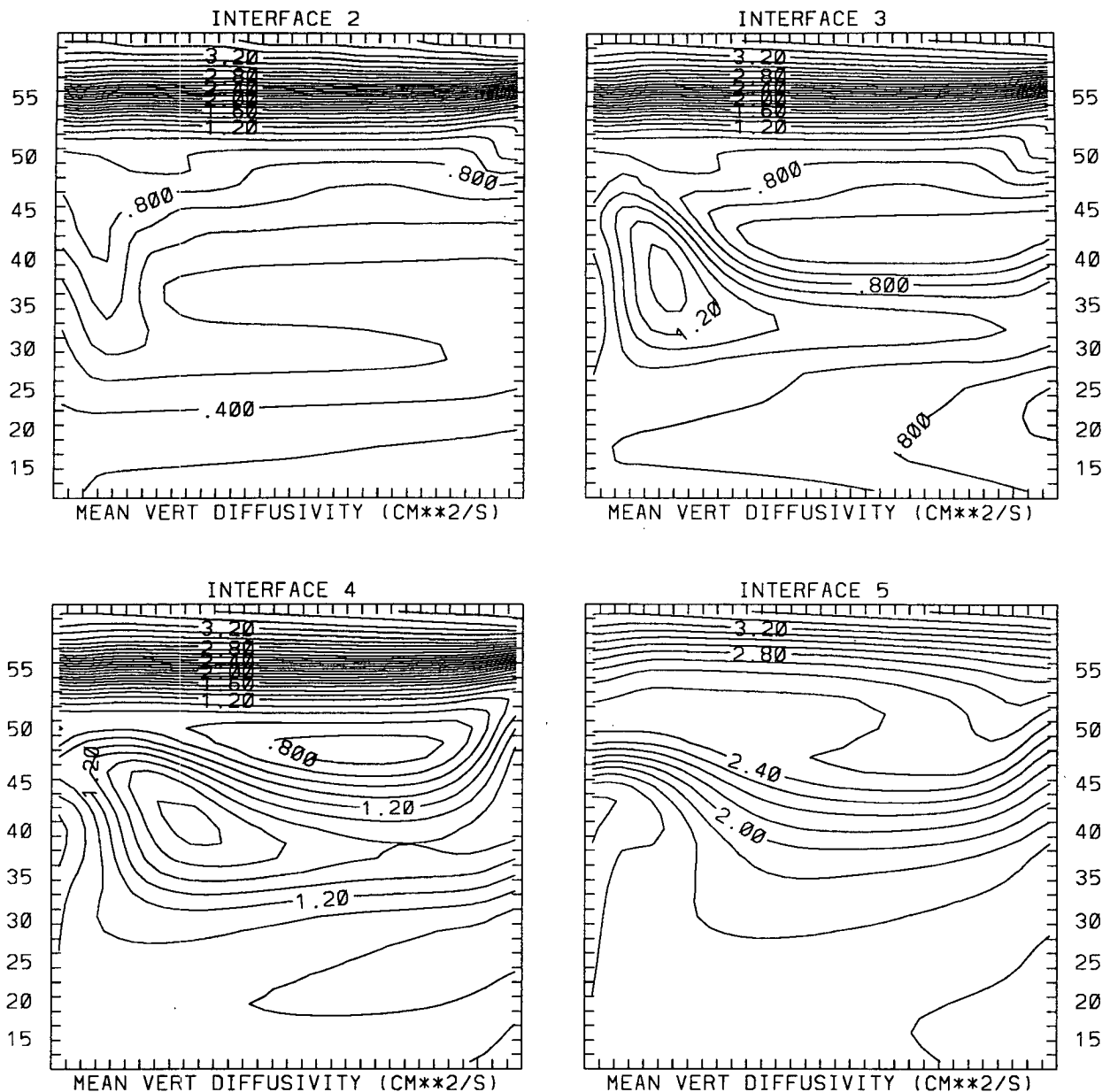


FIG. 2. Annual-mean vertical diffusivity for experiment 3 on interfaces 2–6 (the top interface of layers 2–6). Contour interval: $0.1 \text{ cm}^2 \text{ s}^{-1}$.

As pointed out by Bryan (1987), the relative strengths of wind and thermal forcings in OGCMs can be measured by a nondimensional parameter γ , which is the ratio of a “wind driven” velocity scale U_s to a “thermally driven” velocity scale U_t . Associated with the two velocity scales, there are two depth scales for the thermocline. They are, respectively, an advective depth scale D_a and a diffusive depth scale D_d . For the imposed wind stress and density range at the surface in the present model the wind driven velocity scale and

advective depth scale are respectively 0.66 cm s^{-1} and 161 m. The thermally driven velocity scale and diffusive depth scale are dependent on vertical diffusivity, as is the nondimensional parameter γ . In order to determine U_t , D_d , and γ for the stability-dependent vertical diffusivity experiments, we have chosen two scale values for the vertical diffusivity. One is the vertical average value of the area-averaged AMVD and another is the minimum value of the area-averaged AMVD. Both values are shown in Fig. 3. The corresponding U_t ,

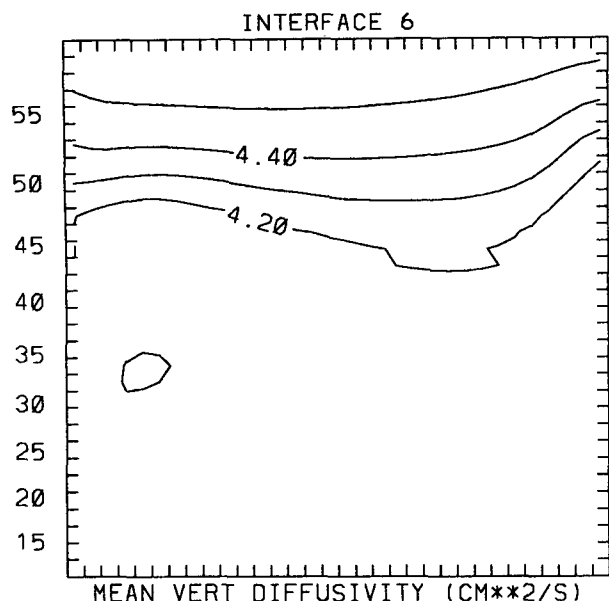


FIG. 2. (Continued)

D_d , and γ are summarized in Table 2, in which \bar{U}_i , \bar{D}_d and $\bar{\gamma}$ are computed from the vertical average values of the area-averaged AMVD, while U_i^* , D_d^* , and γ^* are calculated from the minimum values of the area-averaged AMVD. Note that both $\bar{\gamma}$ and γ^* are larger than unity for experiment 1, indicating that wind forcing dominates over thermal forcing in this experiment.

4. Annual-mean zonally integrated vertical structure and meridional overturning mass transport

In order to derive an expression for the meridional overturning mass transport streamfunction ψ in s coordinates, we rewrite the continuity equation (4) as

$$\nabla_s \cdot \left(\frac{\partial z}{\partial s} \mathbf{v} \right) + \frac{\partial}{\partial s} \left(e + \frac{\partial z}{\partial t} \right) = 0. \quad (11)$$

Integrating (11) zonally over the basin width yields

$$\begin{aligned} \frac{\partial}{\partial \varphi} \int_{\lambda_w}^{\lambda_e} \frac{\partial z}{\partial s} v a \cos \varphi d\lambda \\ + \frac{\partial}{\partial s} \int_{\lambda_s}^{\lambda_e} \left(e + \frac{\partial z}{\partial t} \right) a \cos \varphi d\lambda = 0, \end{aligned} \quad (12)$$

where λ and φ are respectively longitude and latitude, a is the radius of the earth, and λ_w and λ_e are the meridians of the western and eastern boundaries. From (12), ψ can be defined by the following equations:

$$\begin{aligned} \frac{\partial}{\partial s} \psi(\varphi, s, t) &= - \int_{\lambda_w}^{\lambda_e} \frac{\partial z}{\partial s} v a \cos \varphi d\lambda, \\ \frac{\partial}{\partial \varphi} \psi(\varphi, s, t) &= \int_{\lambda_s}^{\lambda_e} \left(e + \frac{\partial z}{\partial t} \right) a \cos \varphi d\lambda. \end{aligned} \quad (13)$$

It follows from (13) that

$$\psi(\varphi, s, t) = - \int_s^{s_0} \int_{\lambda_w}^{\lambda_e} \frac{\partial z}{\partial s'} v a \cos \varphi d\lambda ds', \quad (14)$$

where s_0 is the coordinate surface coinciding with the sea surface. Note that the meridional overturning mass transport streamfunction given by (14) includes not only the contribution from the total diapycnal velocity e but also the contribution from the vertical displacement of the model interfaces $\partial z / \partial t$, which is generally not zero due to the seasonal variation of the surface forcing. For an equilibrium state, however, the annual mean of $\partial z / \partial t$ is zero. Therefore, the advantage of an annual mean meridional streamfunction is that the contribution of $\partial z / \partial t$ is filtered out, and thus the vertical mass transport given by the annual mean meridional overturning streamfunction is only due to diapycnal advection. Using brackets to denote the annual mean, the annual-mean meridional overturning streamfunction can be given as

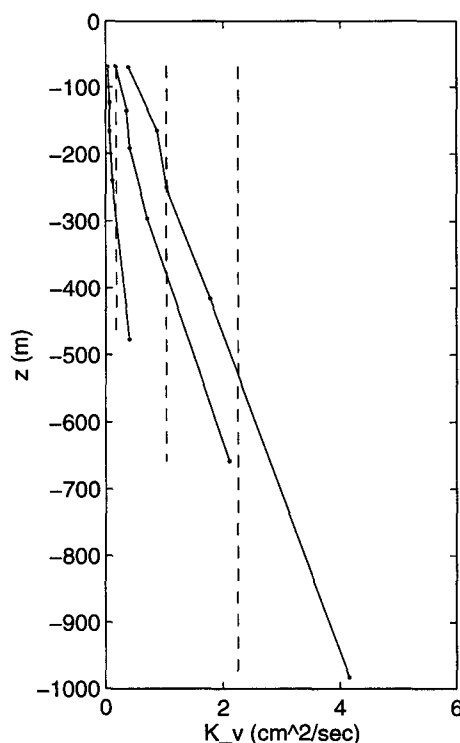


FIG. 3. Vertical profiles of the annual-mean vertical diffusivity (in units of $\text{cm}^2 \text{s}^{-1}$) averaged over the area south of 30°N in the model. From left to right, the solid curves are respectively the profiles for experiments 1, 2, and 3, and the dashed straight lines indicate the mass-weighted vertical average values within the depth ranges of the vertical profiles.

TABLE 2. Summary of velocity and depth scales and nondimensional parameter.

Expt	U_i (cm s ⁻¹)	D_d (m)	γ	\bar{U}_i (cm s ⁻¹)	\bar{D}_d (m)	$\bar{\gamma}$	U_i^* (cm s ⁻¹)	D_d^* (m)	γ^*
1				0.58	140	1.15	0.32	78	2.07
2				1.04	252	0.64	0.57	138	1.17
3				1.35	327	0.49	0.74	181	0.89
4	0.69	167	.97						
5	1.03	249	.65						
6	1.39	338	.48						

$$[\psi](\varphi, s) = - \int_s^{s_0} \int_{\lambda_w}^{\lambda_e} \left[\frac{\partial z}{\partial s'} v \right] a \cos \varphi d\lambda ds'. \quad (15)$$

The annual-mean zonally averaged vertical structure and annual-mean meridional overturning streamfunction $[\psi]$ for experiments 1–6 are shown in Figs. 4–9 and are discussed in detail in the following.

a. Stability-dependent experiments

Figure 4 shows $[\psi]$ for experiment 1, which displays two shallow wind-driven overturning cells and a deep primary overturning cell. In the subtropics, northward and southward Ekman drifts converge at about 35°N where part of the northward flow continues its journey to higher latitudes under the mixed layer, while part of it returns to the south in the upper thermocline. North of 35°N, the equatorward Ekman drift is partially offset by western boundary currents and thus the wind-driven cell is weak compared to that in the south. The deep overturning cell is primarily associated with bottom

water formation at the high latitudes. The transport associated with bottom water formation is about 2 Sv ($\text{Sv} \equiv 10^6 \text{ m}^3 \text{ s}^{-1}$). Due to the low vertical diffusivity, streamlines are sparse in the deep ocean, indicating extremely weak bottom water upwelling. In the upper subtropical thermocline, streamlines are nearly parallel to the isopycnals, indicating that the flow in the thermocline is highly isopycnal. In other words, the thermocline circulation is mainly wind driven. Further, the thermocline is very shallow due to the weak interior diapycnal mixing. Therefore, Fig. 4 displays a picture of thermocline structure and meridional circulation for the case in which surface wind forcing significantly overshadows thermal forcing associated with vertical mixing.

As a_0 increases, the streamlines become denser and more perpendicular to the isopycnals in the upper thermocline (see Figs. 5 and 6), which reflects an increase in the thermally driven circulation. Since more water comes up from deep layers, the wind-driven counterclockwise overturning cell becomes stronger. Aside from the increase in the meridional overturning, the thermocline becomes more diffuse.

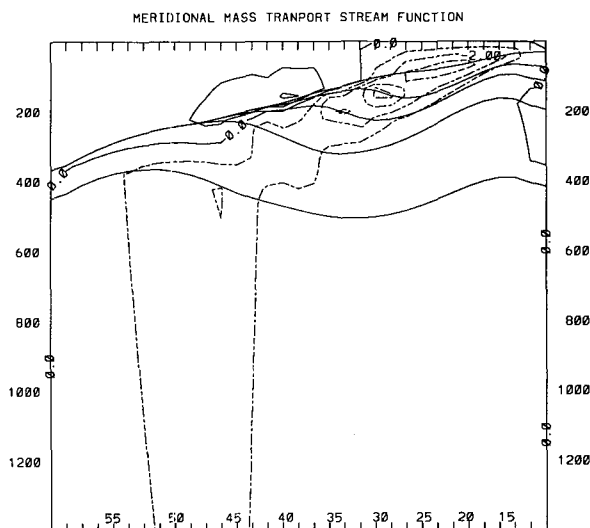


FIG. 4. Annual-mean zonally averaged model interface depths (solid curves) and annual-mean meridional overturning mass transport streamfunction in the latitude–depth plane for experiment 1. Contour interval: $10^6 \text{ m}^3 \text{ s}^{-1}$. Dashed contour lines indicate counterclockwise circulation.

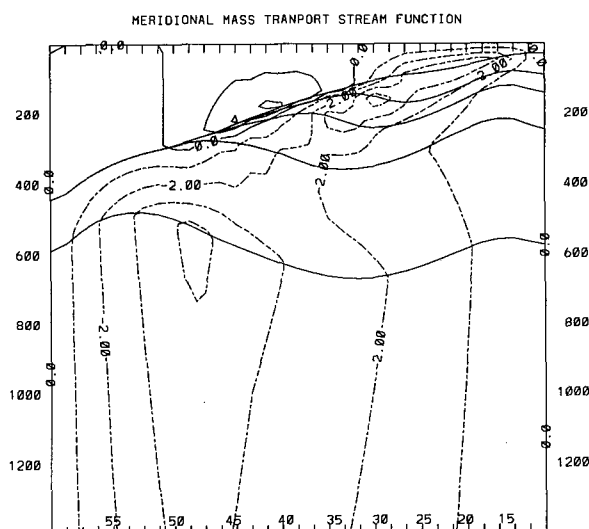


FIG. 5. As in Fig. 4 but for experiment 2.

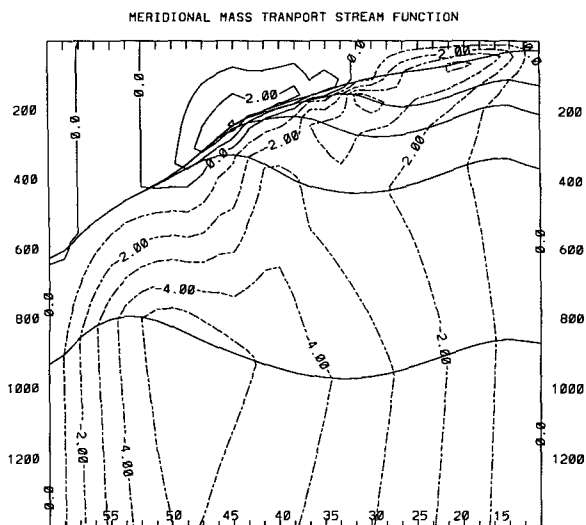


FIG. 6. As in Fig. 4 but for experiment 3.

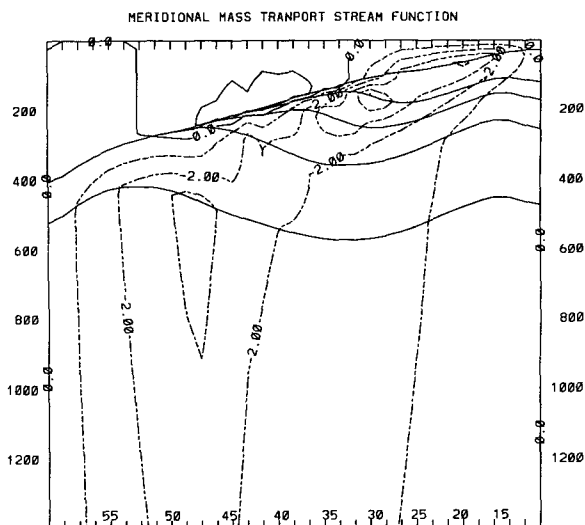


FIG. 7. As in Fig. 4 but for experiment 4.

b. Constant diffusivity experiments

In the constant diffusivity experiments, the overall pattern of the meridional overturning in experiments 4 and 5 is similar to that in all stability-dependent diffusivity experiments. In experiment 6, however, there is an apparent change in the overall pattern. The shallow counterclockwise wind-driven overturning cell in the subtropics is open, and the primary overturning cell at the midlatitudes is now centered at interface 5 rather than at the lowest interface as in the other experiments. In contrast to Fig. 4, which shows wind forcing is dominant in determining the meridional overturning, Fig. 9 displays a case in which meridional overturning is predominantly driven by interior thermal forcing. In Fig. 9, streamlines are much denser than in Fig. 4 and are nearly vertical in the upper subtropical thermocline. Due to the high vertical diffusivity, the thermocline in experiment 6 is too diffuse, and the lowest interface is too deep to be reached by the mixed layer in most time periods of an annual cycle. As a result, more than half of the downward mass transport associated with the primary overturning cell enters layer 5 (5 Sv); only 4 Sv mass transport enters the bottom layer to replace bottom water upwelled in the low latitudes.

c. Constant versus stability-dependent experiments

After describing the sensitivity of the model meridional overturning and thermocline stratification to stability-dependent and constant diffusivities, we proceed to discuss the differences made by the two different types of vertical diffusivities in the model meridional mass transport and vertical stratification. As will be shown in the next section (see Fig. 11), the magnitudes of the meridional heat transport in the present model

are roughly the same for two pairs of the stability-dependent and constant diffusivity experiments: experiments 2 and 4, and experiments 3 and 5. It is therefore interesting to compare the thermocline structure and meridional overturning between these experiments. Comparing Figs. 5 and 6 with Figs. 7 and 8, we note that the maximum mass transports associated with the primary overturning cell are about the same for each pair of experiments. In the upper subtropical thermocline, however, the streamlines are more oriented along the isopycnals in the stability-dependent experiments. Therefore, the stability-dependent parameterization of K_v favors a wind-driven circulation in the upper thermocline. The most pronounced difference between the

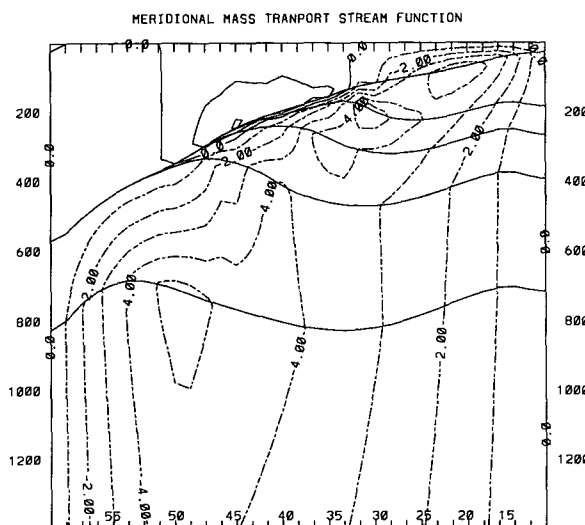


FIG. 8. As in Fig. 4 but for experiment 5.

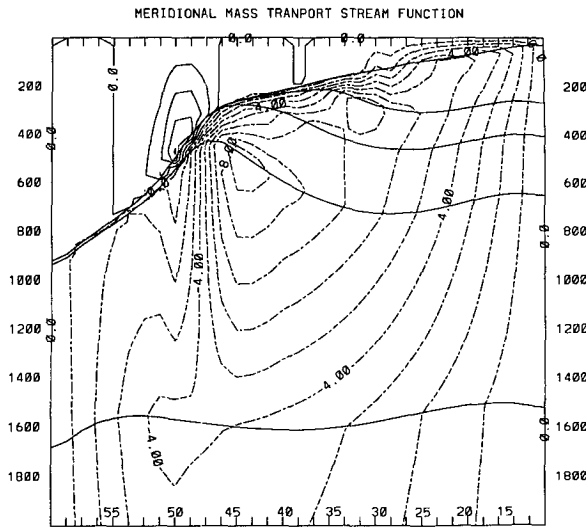


FIG. 9. As in Fig. 4 but for experiment 6.

stability-dependent and constant diffusivity experiments in each pair is in the vertical stratification. In the stability-dependent experiments the vertical stratification in the upper ocean is sharper than that in the constant diffusivity experiments, while in the deep ocean the opposite is true. Comparing the vertical stratification in the two pairs of experiments with that of Levitus, we find that the one in experiment 3 is the best in agreement with the observations, especially in the upper thermocline. In comparison, the upper thermocline in experiment 5 is too diffuse. Nevertheless, the depth of lowest interface ($\sigma_\theta = 27.55$) in experiment 5 remains more shallow than observed. Therefore, constant vertical diffusivity cannot be tuned to obtain realistic vertical stratification for the entire depth of the ocean in the present model.

In section 3 we chose two scale values for the stability-dependent vertical diffusivity to calculate U_v , D_d , and γ . Note that the vertical average values of the area-averaged AMVD in experiment 2 ($1.03 \text{ cm}^2 \text{ s}^{-1}$) and experiment 3 ($2.25 \text{ cm}^2 \text{ s}^{-1}$) are respectively much larger than the values of constant diffusivity in experiment 4 ($0.3 \text{ cm}^2 \text{ s}^{-1}$) and experiment 5 ($1 \text{ cm}^2 \text{ s}^{-1}$). However, the thermoclines in the stability-dependent experiments are much sharper than those in the corresponding constant diffusivity experiments. Therefore, the vertical average diffusivity does not seem to be a relevant scale for the stability-dependent diffusivity in determining the thermocline depth. On the other hand, the minimum values of the area-averaged AMVD in experiments 2 and 3 are respectively 0.18 and 0.38 $\text{cm}^2 \text{ s}^{-1}$, smaller than the corresponding constant diffusivity values in experiments 4 and 5. Thus the minimum values are consistent with the sharper thermocline in the stability-dependent experiments. Using the minimum values one can also reasonably explain why

the strength of the thermocline stratification in experiment 4 is between those in experiments 2 and 3 in that the constant diffusivity in experiment 4 falls between the minimum values of the area-averaged AMVD in the two stability-dependent diffusivity experiments. Therefore, the minimum diffusivity in the vertical is a relevant scale for the stability-dependent diffusivity in determining the thermocline depth.

d. Dependence of the e -folding depth for potential density on vertical diffusivity

In OGCMs the thermocline depth can be described by the e -folding depth for potential density. Bryan (1987) has shown that when the nondimensional parameter γ is not significantly greater than unity, the e -folding depth in the GFDL OGCM is approximately proportional to the $1/3$ power of constant vertical diffusivity as predicted by the diffusive depth scale D_d derived from scaling arguments. The e -folding depth h_e can be computed from the following equation,

$$\sigma_\theta(-h_e) = \sigma_\theta(-H) + \frac{\sigma_\theta(0) - \sigma_\theta(-H)}{e},$$

where H is the basin depth. Dependence of the annual-mean e -folding depth averaged over the area south of 30°N on vertical diffusivity is shown in Fig. 10. In the constant diffusivity case, the e -folding depth is proportional to $K_v^{1/3}$ as predicted by the diffusive depth scale D_d . The e -folding depth also shows a $1/3$ power dependence on the minimum area-averaged AMVD when wind forcing is not dominant. Since wind forcing significantly overshadows the interior thermal forcing in

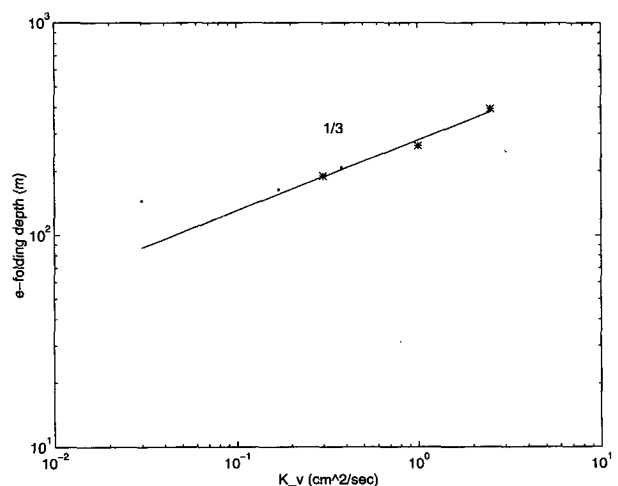


FIG. 10. Dependence of the annual-mean e -folding depth averaged over the area south of 30°N on vertical diffusivity. Vertical axis: depth. Horizontal axis: vertical diffusivity. The stars indicate the data points for the constant diffusivity experiments, and the dots indicate those for the stability-dependent diffusivity experiments (the minimum values of the area-averaged AMVD are used).

experiment 1 ($\gamma^* = 2.07$), it is the only experiment whose e -folding depth cannot be predicted by the $1/3$ power law in this study. By choosing the minimum diffusivity in the vertical, therefore, the $1/3$ power law for the e -folding depth in the constant diffusivity case can be extended to the stability-dependent diffusivity case: the e -folding depth increases with the $1/3$ power of the minimum diffusivity as predicted by the diffusive depth scale D_d^* if γ^* does not significantly exceed unity.

5. Annual-mean meridional heat transport

In the present model, the annual mean meridional heat transport at a latitude φ can be expressed as

$$[F^H](\varphi) = \int_{s_b}^{s_0} \int_{\lambda_w}^{\lambda_e} \rho c_w \left[\left(v\theta - A_{HH} \frac{\partial \theta}{a \partial \varphi} \right) \frac{\partial z}{\partial s} \right] \cos \varphi d\lambda ds. \quad (16)$$

Since equilibrium states are reached in all experiments, the annual mean meridional heat transport $[F^H]$ can also be given as

$$[F^H](\varphi) = \int_{\varphi_s}^{\varphi} \int_{\lambda_w}^{\lambda_e} -[Q] a^2 \cos \varphi' d\lambda d\varphi', \quad (17)$$

where φ_s is the latitude of the southern boundary and Q is positive upward. Equation (17) simply states that the annual-mean northward heat transport across the zonal-vertical section at latitude φ equals the annual mean heat input across the air-sea interface into the basin south of latitude φ . Substituting (8) into (17), we have

$$[F^H](\varphi) = \int_{\varphi_s}^{\varphi} \int_{\lambda_w}^{\lambda_e} \rho c_w \left[\frac{\Delta Z_1}{\tau_R} (T_r(\varphi) - T_1(\lambda, \varphi, t)) \right] \times a^2 \cos \varphi' d\lambda d\varphi'. \quad (18)$$

As shown in Eq. (9), the surface thermal-anomaly damping rate $\Delta Z_1/\tau_R$ is a function of wind speed U_a . In the present model U_a only varies with season and latitude, so $\Delta Z_1/\tau_R$ is independent of longitude. Thus, (18) can be rewritten as

$$[F^H](\varphi) = \int_{\varphi_s}^{\varphi} \rho c_w \left[\frac{\Delta Z_1}{\tau_R} (T_r(\varphi) - \bar{T}_1(\varphi, t)) \right] \times a^2 \cos \varphi' (\lambda_e - \lambda_w) d\varphi', \quad (19)$$

where the overbar denotes a zonal average. For all experiments, the annual-mean meridional heat transports calculated from (16) and (19) are virtually identical.

Dependence of $[F^H]$ in the present model on vertical diffusivity is shown in Fig. 11. In the stability-dependent case, when a_0 is increased by about ten times, the peak value of $[F^H]$ is increased by about 55% from 0.2 pW in experiment 1 to 0.31 pW in experiment 3. In the

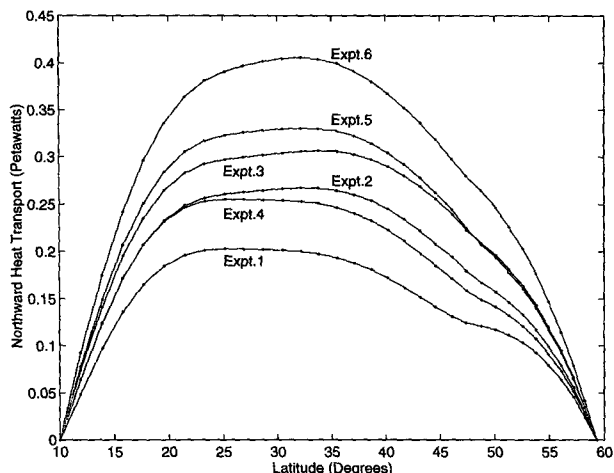


FIG. 11. Dependence of the annual-mean northward heat transport (pW; 1 pW $\equiv 10^{15}$ W) on vertical diffusivity in the isopycnal model.

constant diffusivity case, when the vertical diffusivity is increased by about eight times the peak value of $[F^H]$ is increased by about 58% from 0.26 pW in experiment 4 to 0.41 pW in experiment 6.

To compare the results of the present model with those of the GFDL model, curves of meridional heat transport versus latitude from CHG (1990) and Bryan (1987) are shown in Fig. 12. In the stability-dependent diffusivity case, when a_0 is increased by three times (from 10^{-3} to $3 \times 10^{-3} \text{ cm}^2 \text{ s}^{-2}$) the peak value of the meridional heat transport is about doubled in CHG (see curves for experiment 1 and experiment 1a in Fig. 12a). In the constant diffusivity case, when K_v is increased by five times, the peak value of meridional heat transport is increased by about three times in Bryan (see curves for $K_v = 0.5 \text{ cm}^2 \text{ s}^{-1}$ and $K_v = 2.5 \text{ cm}^2 \text{ s}^{-1}$ in Fig. 12b). Note that in both Bryan and CHG, there is no seasonal cycle in the surface forcings, and thus it is not necessary to distinguish annual-mean and instantaneous meridional heat transport when the model is in equilibrium.

6. Effects of T_r and $\Delta Z_1/\tau_R$ on sensitivity of meridional heat transport to K_v

According to the results in the preceding section, it is obvious that meridional heat transport in the present model is rather insensitive to vertical diffusivity compared with the GFDL model. Many factors may be responsible for the striking difference in the sensitivity of meridional heat transport to K_v between the two models. For example, different model domain, use of isopycnal coordinates, inclusion of the Kraus-Turner mixed-layer model, variable lateral diffusivity, $E - P$ type of surface salinity flux, different surface wind stress, and surface heat flux are all possible candidates. As it turns out, the actual cause of the sensitivity is not

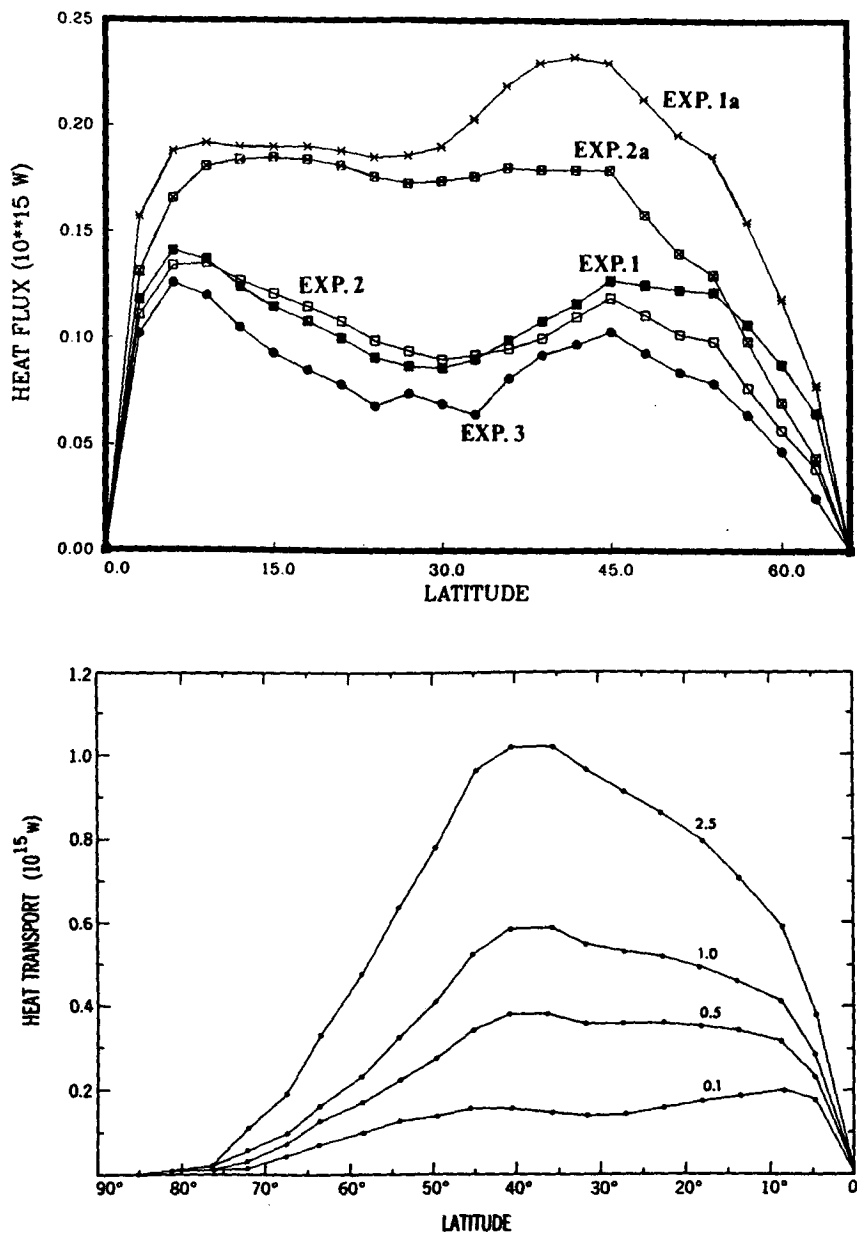


FIG. 12. Dependence of northward heat transport (pW) on vertical diffusivity in the GFDL model adapted from (a) Cummins et al. (1990) and (b) Bryan (1987).

difficult to find. From (17) one notes that if the surface heat flux Q is prescribed, say, from observations, $[F^H]$ should not be sensitive to K_v at all. The fixed Q case, although very special, indicates that sensitivity of $[F^H]$ to K_v is dependent on the way surface heat flux is specified.

In OGCMs surface heat flux is usually parameterized in the Newtonian cooling form (8), so the model $[F^H]$ can be generally given by (19) for an equilibrium state. In this study, we confine our discussion

to the sensitivity of $[F^H]$ given by (19) to vertical diffusivity. For a given model, all parameters in (19) are prescribed except \bar{T}_1 , the model SST. Thus, to various degrees, $[F^H]$ is sensitive to all the processes that can modify the model SST, among which diapycnal mixing is certainly a very important process. However, for different OGCMs that use (8) as a surface thermal boundary condition, the surface heat flux differs not only due to the model SST, but also due to different reference temperature T_r and the ver-

tical damping rate $\Delta Z_1/\tau_R$ used in these models. Besides, T_r and $\Delta Z_1/\tau_R$ also affect the model SST. Since T_r and $\Delta Z_1/\tau_R$ intuitively seem to be important in determining the surface heat flux and thus the meridional heat transport, we proceed to examine how T_r and $\Delta Z_1/\tau_R$ affect the sensitivity of the meridional heat transport to vertical diffusivity.

All data needed in (19) are available for all experiments in the present study. However, $T_r - \bar{T}_1$ data are not directly available from the published results of Bryan and CHG. Thus, we have to indirectly derive them. Differentiating (19) with respect to latitude we have

$$\begin{aligned} \frac{\partial[F^H]}{a\partial\varphi} &= \rho c_w \left[\frac{\Delta Z_1}{\tau_R} (T_r(\varphi) - \bar{T}_1(\varphi, t)) \right] a(\lambda_e - \lambda_w) \cos\varphi \\ &= -[\bar{Q}]a(\lambda_e - \lambda_w) \cos\varphi. \end{aligned} \quad (20)$$

According to (20), it can be inferred whether $[\bar{Q}]$ is downward or upward at a latitude φ from the slope of an $[F^H]$ curve. Further, since $\Delta Z_1/\tau_R$ is a constant and there is no annual cycle in both Bryan and CHG, the annual-mean operator $[\]$ in (20) can be dropped and $T_r - \bar{T}_1$ can be solved as

$$T_r - \bar{T}_1 = \frac{\frac{\partial F^H}{a\partial\varphi}}{\rho c_w \frac{\Delta Z_1}{\tau_R} a(\lambda_w - \lambda_e) \cos\varphi}. \quad (21)$$

With the slopes of F^H curves estimated in Fig. 12, therefore, we can obtain $T_r - \bar{T}_1$ estimates from Eq. (21) for the experiments in Bryan and CHG.

In OGCMs, meridional heat transport is determined by various processes. To facilitate a sensitivity analysis, we start with isolating the effect of vertical diffusivity on meridional heat transport in OGCMs. To this end, we divide the temperature difference in the integrand of (19) into two parts, that is,

$$T_r(\varphi) - \bar{T}_1(\varphi, t) = (T_r(\varphi) - \bar{T}_1^{\text{wind}}(\varphi, t)) + (\bar{T}_1^{\text{wind}}(\varphi, t) - \bar{T}_1(\varphi, t)).$$

Strictly speaking, \bar{T}_1^{wind} should be the model SST when vertical diffusivity is zero and \bar{T}_1 the model SST when vertical mixing is added in order to completely isolate the effect of vertical diffusivity. In the present study we regard \bar{T}_1^{wind} as the model SST when the wind forcing significantly outweighs the interior thermal forcing associated with vertical diffusivity. The meridional heat transport, therefore, can be correspondingly divided into the transport driven by wind and that driven by vertical diffusivity; that is,

$$\begin{aligned} [F^H](\varphi) &= [F_{\text{wind}}^H](\varphi) + [F_{\text{diff}}^H](\varphi) = \int_{\varphi_s}^{\varphi} \rho c_w \left[\frac{\Delta Z_1}{\tau_R} (T_r(\varphi) - \bar{T}_1^{\text{wind}}(\varphi, t)) \right] a^2 \cos\varphi' (\lambda_e - \lambda_w) d\varphi' \\ &\quad + \int_{\varphi_s}^{\varphi} \rho c_w \left[\frac{\Delta Z_1}{\tau_R} (\bar{T}_1^{\text{wind}}(\varphi, t) - \bar{T}_1(\varphi, t)) \right] a^2 \cos\varphi' (\lambda_e - \lambda_w) d\varphi'. \end{aligned}$$

Since the effect of vertical diffusivity on meridional heat transport is measured based on $[F_{\text{wind}}^H]$, our next step is to compare and analyze $[F_{\text{wind}}^H]$ in the two models. As discussed in section 4, in the present study experiment 1 ($K_v = 5.75 \times 10^{-4} \text{N}^{-1}$) is the only experiment in which wind forcing is significantly dominant over the interior thermal forcing ($\gamma^* = 2.07$). We also regard experiment 1 in CHG ($K_v = 10^{-3} \text{N}^{-1}$) as the wind-forcing dominant experiment since the proportionality coefficient a_0 is only about 40% larger. In Bryan, the experiment with K_v equal to $0.1 \text{ cm}^2 \text{ s}^{-1}$ is the one in which wind forcing is dominant ($\gamma = 1.6$). Therefore, $[F^H]$ and \bar{T}_1 in these three wind-forcing dominant experiments are considered as $[F_{\text{wind}}^H]$ and \bar{T}_1^{wind} in our discussion.

From the heat transport curve for experiment 1 in Fig. 12a and the lowest curve in Fig. 12b, we note that the GFDL model only gains heat in the first two grid boxes counting from the equator in the low latitudes.

In other words, \bar{T}_1 is higher than T_r in the low latitudes except in a narrow equatorial zone. Note that T_r is the zonally averaged observed SST in both Bryan and CHG. Therefore, whether the model ocean gains or loses heat at a given latitude solely depends on whether the model SST is greater or less than the observed SST. When the effect of vertical diffusivity is negligibly small, the major factor that drives \bar{T}_1 down below the observed SST in the low latitudes is the wind-driven upwelling near the equator. That is why the downward heat flux zone is so narrow in the wind-forcing dominant experiments with the GFDL model. On the other hand, $\Delta Z_1/\tau_R$ is large (2 m day^{-1}) in both CHG and Bryan, which tends to tie the model SST closely to the observed SST. As a result, $T_r - \bar{T}_1$ is small even in the region of strong upwelling. In fact, $T_r - \bar{T}_1$ is about 0.78°C in the first row of grid boxes (for simplicity, first grid box hereafter) for experiment 1 in CHG. The $T_r - \bar{T}_1$ value is calculated from (21), where we have

used $\rho = 1 \text{ g cm}^{-3}$, $c_w = 4 \text{ J g}^{-1} \text{ K}^{-1}$, $\Delta Z_1/\tau_R = 0.0023 \text{ cm s}^{-1}$, $a = 6370 \times 10^5 \text{ cm}$, $\lambda_w - \lambda_e = 45^\circ$, $\cos \varphi = 1$, and $\partial F^H/a\partial\varphi$ is estimated from the curve for experiment 1 in Fig. 12a as

$$\begin{aligned} \frac{\partial F^H}{a\partial\varphi} &= \frac{0.12 \times 10^{15} \text{ W}}{6370 \times 10^5 \text{ cm} \times 3^\circ \times \pi/180^\circ} \\ &= 3.6 \times 10^6 \text{ W cm}^{-1}. \end{aligned}$$

Similarly we obtain $T_r - \bar{T}_1 = 0.58^\circ\text{C}$ for the first grid box in the wind-forcing dominant experiment in Bryan.

In the present model, the reference temperature T_r is the SST resulting from a balance between turbulent and radiative heat fluxes for a motionless ocean with zero thermal inertia (BHHK 1989). As in BHHK we denote this SST by T_{flux} . Figures 13 and 14a show the annual variation of T_{flux} and \bar{T}_1 for experiment 1, respectively. Since the model ocean is in motion and its thermal inertia is large, it is not surprising that T_{flux} is much higher than \bar{T}_1 in the low latitudes. Intercomparison of Figs. 13 and 14a indicates that $T_{\text{flux}} - \bar{T}_1$ can be as large as 5°C in the first grid box counting from the southern boundary in experiment 1. Note that the large temperature difference may also due to the small vertical damping rate $\Delta Z/\tau_R$ in the present model, which, in the first grid box, is only about one-tenth of that in CHG and Bryan. On the other hand, contribution of the large temperature difference $T_{\text{flux}} - \bar{T}_1$ to $[Q]$ is reduced by the small $\Delta Z/\tau_R$. The fact that the peak value of $[F^H]$ in experiment 1 is larger than that in experiment 1 of CHG is not due to the intensity of the downward heat flux in the present model. In fact, the slope of the $[F^H]$ curve in experiment 1 in the first grid box is smaller than that in experiment 1 of CGH, indicating less heat gain near the southern boundary in the present model. Therefore, it is the larger latitude coverage of the downward heat flux in experiment 1 that results in the larger meridional heat transport.

As vertical diffusivity increases, wind forcing is no longer the only major factor in driving down the model SST. Since \bar{T}_1 is now forced down by the increased vertical mixing in the subtropics, Fig. 12 shows that the area of downward heat flux in the low latitudes is extending northward with increasing vertical diffusivity in both CHG and Bryan, no longer confined to the narrow equatorial upwelling zone. We can approximately examine the net effect of vertical diffusivity on meridional heat transport by comparing the difference in $[F^H]$ between the thermal-forcing dominant and wind-forcing dominant experiments. For both models, experiments with K_v equal to $2.5 \text{ cm}^2 \text{ s}^{-1}$ are thermal-forcing dominant. From the top curve in Fig. 12b and Eq. (21), we obtain that $T_r - \bar{T}_1$ in the first grid box is about 1.23°C for the thermal-forcing dominant experiment ($K_v = 2.5 \text{ cm}^2 \text{ s}^{-1}$) in Bryan. Remember $T_r - \bar{T}_1^{\text{wind}}$ in this box is about 0.58°C . This means that $\bar{T}_1^{\text{wind}} - \bar{T}_1$ is about 0.65°C . In the present model, on the other hand, \bar{T}_1 in the thermal-forcing dominant exper-

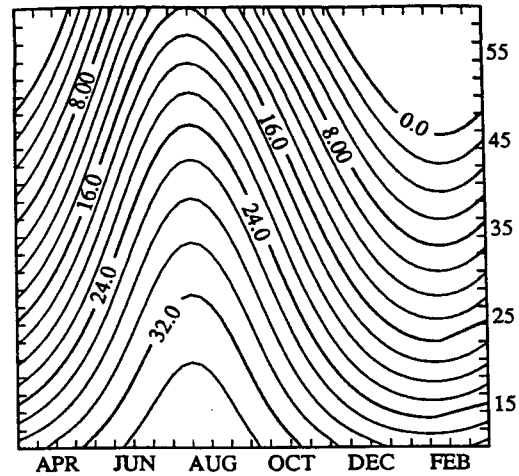


FIG. 13. Annual variation of the reference temperature T_{flux} ($^\circ\text{C}$) used in the isopycnal model (adapted from Bleck et al. 1989).

iment (expt. 6) is about 2°C lower than in the wind-forcing dominant experiment (expt. 1) near the southern boundary (see Fig. 14). Note that sensitivity in the meridional heat transport is not determined by the absolute magnitude of $\bar{T}_1^{\text{wind}} - \bar{T}_1$, but by the ratio of $\bar{T}_1^{\text{wind}} - \bar{T}_1$ to $T_r - \bar{T}_1^{\text{wind}}$. In the first grid box counting from the southern boundary, $\bar{T}_1^{\text{wind}} - \bar{T}_1$ is only about 40% of $T_r - \bar{T}_1^{\text{wind}}$ in the present model, but about 112% of $T_r - \bar{T}_1^{\text{wind}}$ in Bryan. Further, meridional heat transport in Bryan is enhanced by the disappearance of the heat loss region in the subtropics. As a result, meridional heat transport is highly sensitive to the magnitude of vertical diffusivity. In comparison, the sensitivity is low in the present model.

According to the above discussion, it is clear that the difference in the sensitivity of meridional heat transport between the two models is mainly due to the model differences in T_r and $\Delta Z/\tau_R$. In the GFDL model, the model SST is relaxed to the observed SST, so the model ocean does not gain heat in the low latitudes unless the model SST is driven down below the observed SST. Further, the large surface anomaly damping rate $\Delta Z/\tau_R$ in the model considerably offsets the cooling effect of wind-driven upwelling. All these combined make the temperature difference $T_r - \bar{T}_1$ very small and make the region of downward heat flux confined to a narrow equatorial zone in the low latitudes when vertical diffusivity is negligibly small. In contrast, the reference temperature T_{flux} in the present model is derived from the balance of observed sensible, latent, and radiative heat fluxes assuming the ocean has no motion and no thermal inertia. This implies that T_{flux} is inherently higher than the observed SST in the region where the total observed heat flux is downward in the low latitudes. Thus a positive $T_r - \bar{T}_1$ can be obtained in the subtropics when vertical diffusivity is extremely low in that for a negative $T_r - \bar{T}_1$, the model SST must be

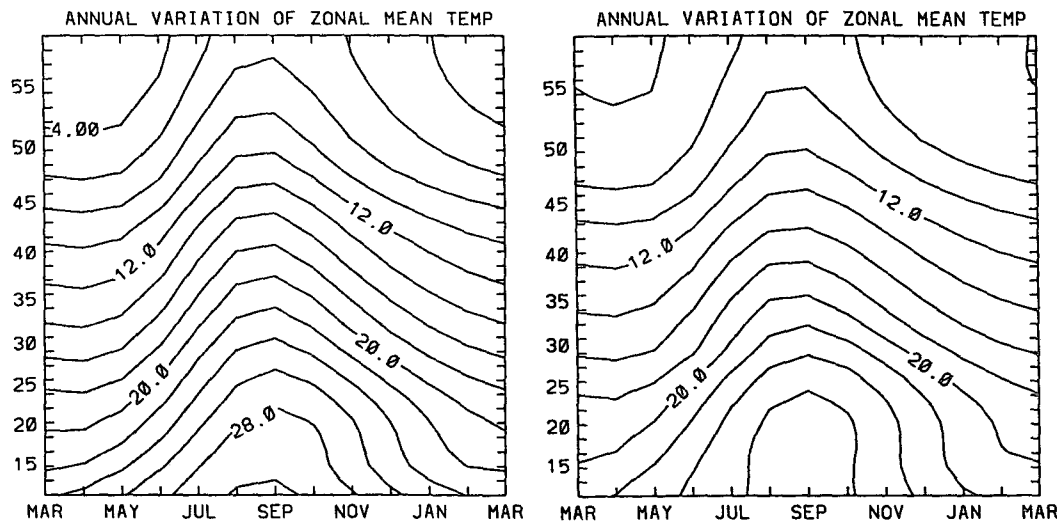


FIG. 14. Annual variation of zonally averaged sea surface temperature ($^{\circ}\text{C}$) for (a) experiment 1 and (b) for experiment 6.

driven up above the high T_{flux} rather than the observed SST. Further, the small $\Delta Z/\tau_R$ in the model does not offset the surface cooling associated with the wind-driven upwelling very much. As a result, $T_r - \bar{T}_1^{\text{wind}}$ is large in magnitude and the region of the downward heat flux in the low latitudes is broad when vertical mixing is very weak. It is the basic differences in the magnitude and distribution of $T_r - \bar{T}_1^{\text{wind}}$ associated with different model T_r and $\Delta Z/\tau_R$ that result in the model difference in the sensitivity of meridional heat transport to vertical diffusivity. Due to the large $T_r - \bar{T}_1^{\text{wind}}$ in the present model, further decrease in the model SST, or $\bar{T}_1^{\text{wind}} - \bar{T}_1$, due to high vertical mixing is only a small fraction of it even though the magnitude of $\bar{T}_1^{\text{wind}} - \bar{T}_1$ is larger than that in the GFDL model. In contrast, $T_r - \bar{T}_1^{\text{wind}}$ is small in the GFDL model, so $\bar{T}_1^{\text{wind}} - \bar{T}_1$ due to high vertical diffusivity can be as large as $T_r - \bar{T}_1^{\text{wind}}$ itself. Further, in the subtropical heat-loss region, the high damping rate $\Delta Z/\tau_R$ tends to force the higher \bar{T}_1 back to the observed SST and thus helps the vertical mixing to eliminate the heat loss in the low latitudes. As a result, the absolute decrease in \bar{T}_1 due to high vertical diffusivity in the GFDL model is larger than that in the present model, which enhances the meridional heat transport in the GFDL model since F^H reflects the integral effect of the surface heat flux.

7. Summary and conclusions

Solutions of OGCMs depend upon parameterizations of subgrid-scale mixing processes because the processes act as forcing/dissipating terms in the governing equations. Understanding the role of each parameterized process in determining the OGCM solutions is thus very important for the model improvement. In this paper we investigate what is behind the sensitivity of thermocline

depth and meridional heat transport in OGCMs. Our results and conclusions can be summarized as follows.

1) The thermocline depth and structure in the present model is sensitive to vertical diffusivity both in magnitude and in type. The e -folding depth for potential density is proportional to the $1/3$ power of vertical diffusivity in the constant diffusivity experiments. This agrees with the results of both model experiments and scaling analysis in Bryan. In the stability-dependent vertical diffusivity experiments, it is found that the minimum diffusivity in the vertical is a relevant scale for the vertical diffusivity in determining the depth of the thermocline. Plotting against the minimum diffusivities, the e -folding depths in the stability-dependent experiments also show a $1/3$ power dependence except the one in which wind forcing significantly outweighs the interior thermal forcing. With the diffusivity scale determined by the minimum diffusivity, therefore, the $1/3$ power law derived from the scaling analysis for the thermocline depth can be extended to the stability-dependent diffusivity case. As far as vertical stratification is concerned, the stability-dependent parameterization is clearly better than the constant diffusivity parameterization. Constant diffusivity tends to produce a diffuse upper thermocline and cannot be tuned to obtain a reasonable stratification for the entire depth in the present model. The results of this study suggest that a stability-dependent vertical diffusivity be used in OGCMs.

2) Meridional heat transport in the present model is relatively insensitive to vertical diffusivity compared to the GFDL model. It is shown that the model sensitivity difference is mainly due to the model difference in the reference temperature T_r and the surface anomaly damping rate $\Delta Z_1/\tau_R$ used in the Newtonian cooling-type surface heat flux parameterization. Thus, high sensitivity of

meridional heat transport to vertical diffusivity can be reduced by appropriate choice of T_r and $\Delta Z_1/\tau_R$.

3) There is a difference between the effect of vertical diffusivity on thermocline stratification and on meridional heat transport in OGCMs. The fact that the e -folding depth can be predicted by the $1/3$ power law both in the GFDL model and the present model for the constant diffusivity case indicates that the effect of vertical diffusivity on thermocline stratification is relatively independent of parameterizations of other processes. On the other hand, the effect of vertical diffusivity on meridional heat transport depends greatly on parameterizations of surface heat flux and the processes that affect model SST. Therefore, it is advisable to tune the vertical diffusivity parameterization to produce realistic thermocline structure and leave the task of simulating meridional heat transport to the parameterization of surface heat flux and other processes.

Acknowledgments. The author would like to thank Dr. Rainer Bleck for reading the early versions of this paper and his valuable comments. This research was supported 50% by a grant from the Department of Energy National Institute for Global Environmental Change and 50% by a grant from the NOAA Office of Global Programs to the Hayes Center at JISAO. All computations in this paper were carried out on the Dec-alpha workstations at the JISAO.

REFERENCES

- Bleck, R., H. P. Hanson, D. Hu, and E. B. Kraus, 1989: Mixed layer-thermocline interaction in a three-dimensional isopycnal coordinate model. *J. Phys. Oceanogr.*, **19**, 1417–1439.
- , C. Rooth, D. Hu, and L. T. Smith, 1992: Salinity-driven thermocline transients in a wind- and thermohaline-forced isopycnal coordinate model of the North Atlantic. *J. Phys. Oceanogr.*, **22**, 1486–1505.
- Bryan, F., 1987: Parameter sensitivity of primitive equation ocean general circulation models. *J. Phys. Oceanogr.*, **17**, 970–985.
- Cummins, P. F., G. Holloway, and A. E. Gargett, 1990: Sensitivity of the GFDL general circulation model to a parameterization of vertical diffusion. *J. Phys. Oceanogr.*, **20**, 817–830.
- Gargett, A. E., 1984: Vertical eddy diffusivity in the ocean interior. *J. Mar. Res.*, **42**, 359–393.
- Gregg, M. C., 1987: Diapycnal mixing in the thermocline: A review. *J. Geophys. Res.*, **92C**, 5249–5286.
- Haney, R. L., 1971: Surface thermal boundary condition for ocean circulation models. *J. Phys. Oceanogr.*, **1**, 241–248.
- Hu, D., 1991: Diapycnal mixing in a joint mixed-layer/isopycnal coordinate model of wind- and thermohaline-driven ocean general circulation. Ph.D. dissertation, University of Miami, 201 pp.
- , 1996: The computation of diapycnal diffusive and advective scalar fluxes in multilayer isopycnal-coordinate ocean model. *Mon. Wea. Rev.*, **124**, 1834–1851.
- Kraus, E. B., 1990: Diapycnal mixing. *Climate–Ocean Interaction*, M. E. Schlesinger, Ed., Kluwer Academic, 269–293.
- Levitus, S., 1982: *Climatological Atlas of the World Ocean*. NOAA Prof. Paper No. 13, U.S. Govt. Printing Office, 173 pp.
- McDougall, T. J., 1987: Thermobaricity, cabbeling, and water-mass conversion. *J. Geophys. Res.*, **92**, 5448–5464.
- Moum, J. N., and T. R. Osborn, 1986: Mixing in the main thermocline. *J. Phys. Oceanogr.*, **16**, 1250–1259.
- Muller, P., and G. Holloway, 1989: Parameterization of small scale processes. *Eos, Trans. Amer. Geophys. Union*, **70**, 818–830.
- Schmitt, R. W., P. S. Bogden, and C. E. Dorman, 1989: Evaporation minus precipitation and density fluxes for the North Atlantic. *J. Phys. Oceanogr.*, **19**, 1208–1221.
- Smagorinsky, J. S., 1963: General circulation experiments with the primitive equations. I: The basic experiment. *Mon. Wea. Rev.*, **91**, 99–164.